Widespread CO2 and CO ices in the trans-Neptunian population revealed by JWST/DiSCo-TNOs

Mário de Prá, Elsa Hénault, Noemí Pinilla-Alonso, Bryan Holler, Rosario Brunetto, John Stansberry, Ana Carolina de Souza Feliciano, Jorge Carvano, Brittany Harvison, Javier Licandro, et al.

Widespread CO2 and CO in the Trans-Neptunian Population revealed by JWST/DiSCo-TNOs

Elsa Hénault
Université Paris-Saclay
Noemi Pinilla-Alonso
University of Central Florida https://orcid.org/0000-0002-2770-7896
Bryan Holler
Space Telescope Science Institute
Rosario Brunetto
Institut d'Astrophysique Spatiale https://orcid.org/0000-0003-3001-9362
Ana Carolina de Souza Feliciano
Florida Space Institute
John Stansberry
Space Telescope Science Institute https://orcid.org/0000-0003-2434-5225
Brittany Harvison
University of Central Florida
Thomas Müller
Max-Planck-Institut für extraterrestrische Physik https://orcid.org/0000-0002-0717-0462
Michele Bannister
University of Canterbury
Dale Cruikshank
University of Central Florida https://orcid.org/0000-0002-0541-5569
Joshua Emery
Northern Arizona University https://orcid.org/0000-0001-9265-9475
Aurélie Guilbert-Lepoutre
Laboratoire de Géologie de Lyon: Terre, Planètes, Environnement
Javier Licandro
Instituto de Astrofisica de Canarias
Vania Lorenzi
Fundacion Galileo Galilei - INAF
Nuno Peixinho
Instituto de Astrofísica e Ciências do Espaço, Departamento de Física https://orcid.org/0000-0002-6830-476X
Yvonne Pendleton
University of Central Florida https://orcid.org/0000-0001-8102-2903

Charles Schambeau
University of Central Florida
Mario De Pra
mariondepra@gmail.com

University of Central Florida https://orcid.org/0000-0001-8746-6468

Article

Keywords:

Posted Date: May 19th, 2023

DOI: https://doi.org/10.21203/rs.3.rs-2887978/v1

Additional Declarations: There is **NO** Competing Interest.

Version of Record: A version of this preprint was published at Nature Astronomy on May 22nd, 2024. See the published version at https://doi.org/10.1038/s41550-024-02276-x.

Widespread CO_2 and CO in the Trans-Neptunian Population revealed by JWST/DiSCo-TNOs

Mário N. De Prá[1,*], Elsa Hénault[2], Noemí Pinilla-Alonso[1], Bryan J. Holler[3], Rosario Brunetto[2], Ana Carolina de Souza Feliciano[1], John A. Stansberry[3], Brittany Harvison[1], Thomas G. Müller[4], Michele T. Bannister[5], Dale P. Cruikshank[6], Joshua P. Emery[7], Aurélie Guilbert-Lepoutre[8], Javier Licandro[9,10], Vania Lorenzi[9,11], Nuno Peixinho[12], Yvonne J. Pendleton[6], and Charles A. Schambeau[1]

[1]Florida Space Institute, University of Central Florida, Orlando, FL, USA
[*]mariodepra@ucf.edu
[2]Université Paris-Saclay, CNRS, Institut d'Astrophysique Spatiale, Orsay, France
[3]Space Telescope Science Institute, Baltimore, MD, USA
[4]Max-Planck-Institut für extraterrestrische Physik, Garching, Germany
[5]University of Canterbury, School of Physical and Chemical Sciences – Te Kura Matū, Christchurch, New Zealand
[6]University of Central Florida, Department of Physics, Orlando, FL, USA
[7]Northern Arizona University, Flagstaff, AZ, USA
[8]Laboratoire de Géologie de Lyon: Terre, Planètes, Environnement, CNRS, UCBL, ENSL, Villeurbanne, France
[9]Instituto de Astrofisica de Canarias, La Laguna, Tenerife, Spain
[10]Universidad de La Laguna, Departamento de Astrofisica, La Laguna, Tenerife, Spain
[11]Fundación Galileo Galilei-INAF, Tenerife, Spain
[12]Instituto de Astrofísica e Ciências do Espaço, Departamento de Física, Universidade de Coimbra, Portugal

ABSTRACT

Carbon dioxide (CO_2) is one of the most abundant ices in the solar system. It has been detected in giant planet atmospheres and on their moons, on and around comets, and even in regions of Mercury, the Moon, and Mars. However, despite their formation in the coldest regions of the protoplanetary disk, CO_2 was not previously detected on trans-Neptunian objects (TNOs). Carbon monoxide (CO) was only expected to be present in the largest TNOs. Out of 45 total, we report the detection of both CO_2 and CO in 42 and 24 TNOs, respectively, observed with the NIRSpec instrument on the JWST by the DiSCo-TNOs project (PID 2418). Our analysis shows that CO_2 is widespread in the trans-Neptunian region, independent of dynamical class, while CO is a common constituent of the reddest objects in our sample. The abundance and characteristics of CO_2 suggest that most of it could be primordially accreted. While, CO is probably being produced by ion irradiation of CO_2 and other C-bearing species. Our results suggest the prevalence of two compositional groups among TNOs based on the abundance and properties of CO_2 and CO. We discuss the implication of these results in the context of solar system formation.

Introduction

The population of icy planetesimals found beyond the orbit of Neptune (semi-major axis, $a > 30.1$ au), commonly referred to as trans-Neptunian onobjects (TNOs), are ideal laboratories for studying the original composition of the protoplanetary disk. TNOs have surface temperatures below $\sim$50 K, which allows them to retain a wide range of ices, depending on their size and orbit[1–3]. The largest and coldest objects are expected to retain their original inventories of even those ices that are volatile at these temperatures, which include N_2, CO, and CH_4[4]. On the other hand, the vast majority of the more than 4000 currently known TNOs are too small or too warm to retain significant amounts of volatile ices and should retain only non-volatiles, which at these temperatures could include CO_2, H_2S (hydrogen sulfide), NH_3 (ammonia), SO_2 (sulfur dioxide), CH_3OH (methanol), and H_2O, along with refractory organic compounds and silicates.

The red colors of many TNOs support the presence of refractory organic compounds[5–8], while robust detections of H_2O ice have been previously reported for many TNOs in the literature[9–11]. Possible detections of CH_3OH have been made for a handful of small objects[12–14]. Sulfur-bearing compounds have yet to be reported on any TNO and the possible presence of CO, NH_3, and related compounds has only been reported within the Pluto system[15,16]. Surprisingly, definitive detection of CO_2 ice on TNOs has remained elusive. CO_2 is a ubiquitous ice species found throughout the solar system[17], having been identified

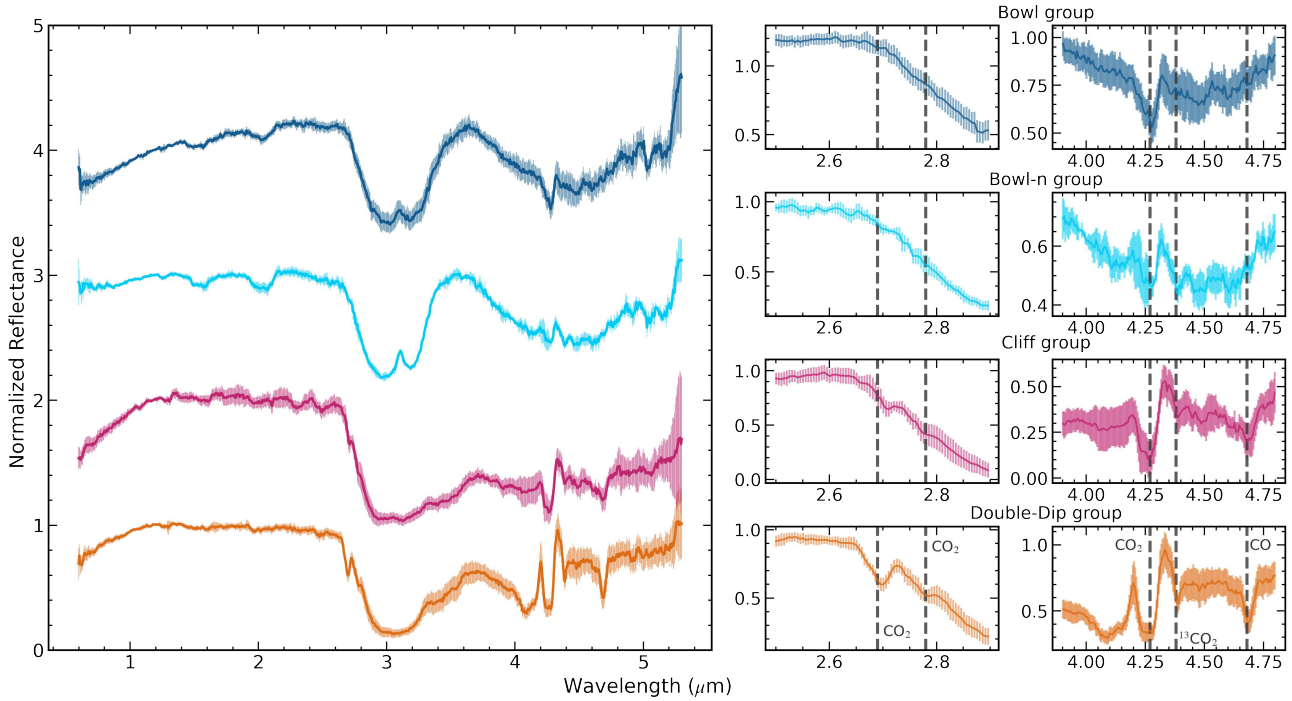

Figure 1. *left*: Median spectra of the groups identified by Pinilla-Alonso et al. (in prep.): Bowl (dark blue), Bowl-n (light blue), Cliff (magenta), Double-Dip (orange). *right*: Zoomed spectra at the wavelength regions where the fundamental (4.27 μm) and overtone (2.68 μm and 2.78 μm) features of CO_2, the $^{13}CO_2$ isotope at 4.36 μm, and the CO feature at 4.68 μm are present. Error bars show the standard deviation within a group.

even on Mercury and the Moon in shadowed craters[18,19]; polar caps on Mars[20]; throughout the satellite systems of Jupiter, Saturn, and Uranus[21–25]; gas comae of comets and centaurs[26]; and on Neptune's largest moon Triton[27,28], a captured TNO[29].

Possible reasons for the lack of previous detections of CO_2 on TNOs include a lower abundance of CO_2 due to post-accretional processes at the formation distances of TNOs, CO_2 becoming buried under layers of other ices over time, conversion into other molecules through irradiation, and simple observational limitations (i.e., inadequate signal-to-noise, spectral resolving power, and/or spectral range). Due to their faintness, it is challenging to obtain spectra of many TNOs from the ground, and on top of that the Earth's atmosphere makes it challenging to perform observations at wavelengths longer than $\sim$2.5 μm. CO_2 absorption features are present in this region at $\sim$1.965, 2.01, and 2.07 μm, as observed on the classical Uranian satellites and Triton[22,25,28], but the low resolving power needed to obtain any kind of usable signal-to-noise ratio (SNR) on the majority of TNOs prevents the detection of these bands. Stronger CO_2 bands are found at wavelengths longward of 2.5 μm and inaccessible from the ground, with the fundamental absorption feature of pure CO_2 at $\sim$4.27 μm and overtones at 2.68 and 2.78 μm.

To access these long-wavelength absorption features of CO_2, and to obtain adequate signal-to-noise ratio and spectral resolution, on TNOs that can not be observed from the ground, requires a space-based near-infrared facility such as the James Webb Space Telescope (JWST). In this work, we investigated the infrared spectra of 45 TNOs obtained as part of the JWST Large Cycle 1 GO project "Discovering the Composition of the Trans-Neptunian Objects, Icy Embryos for Planet Formation" (DiSCo-TNOs; PID 2418). The data were obtained with the NIRSpec Integral Field Unit (IFU) using the Prism/CLEAR combination, providing low-resolving power spectra (R$\sim$30-300) in the wavelength range between 0.6 – 5.3 μm[30]. Additional details about the data acquisition and reduction can be found in Pinilla-Alonso et al. (in prep, hereafter referred to as NPA23). The remainder of this paper explores the presence and characteristics of the CO_2 and CO ice features on 42 TNOs as a means of constraining their volatile content and, by extension, their initial conditions in the solar nebula.

Results

We inspected each spectrum of the sample individually, looking for signatures of the fundamental feature of pure CO_2 at 4.27 μm, the overtone features of pure CO_2 at 2.68 μm and 2.78 μm, the $^{13}CO_2$ isotope at 4.36 μm, and the CO feature at 4.68 μm. Out of the spectra of 45 objects analyzed, 42 exhibited signatures of CO_2, with the exception of the 3 misfits: Centaurs 52872 Okyrhoe (1998 SG_{35}) and 310071 (2010 KR_{59}), and the Haumea family member 416400 (2003 UZ_{117}), which are

not included in the remaining of this work. Out of these objects, 24 also present the CO feature, typically coupled with the additional presence of CO_2 overtone and $^{13}CO_2$ features. The detection of the CO feature was considered dubious or marginal for 5 additional objects. Fig. 1 shows the average spectra of the four groups of TNOs identified by NPA23 based on the spectral signatures from 0.65 to 5.1 μm, and named based on the structure of the 3-μm absorption band: Bowl, Bowl-n, Double-Dip, and Cliff (see Section). The presence, strength, and shape of the CO_2 and CO features are highly correlated within these groups, with the Bowl and Bowl-n types only weakly showing the fundamental CO_2 feature, while the Double-Dip and Cliff types typically showing also the CO_2 overtones, the $^{13}CO_2$ isotope, and the CO fundamental features. Interestingly, the spectra of the Double-Dip objects display "enhanced" wing-peaks on the short- and long-wavelength of the 4.27 μm ice band, while the majority of Cliff types only show the long-wavelength enhancement. Moreover, some Cliff objects present a weaker CO_2 fundamental feature, with a more "usual" band shape, similar to those in the Bowl and Bowl-n groups.

Distribution and properties of CO_2 among TNOs

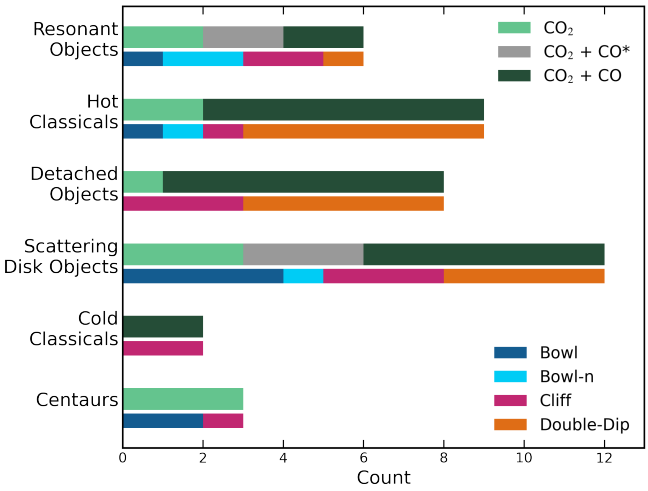

Figure 2. Distribution of CO_2 and CO detections, and of NPA23 spectral groups, by dynamical groups. All Double-Dip objects present both CO_2 and CO features, while some Cliff types do not show the latter. Bowl and Bowl-n groups only show robust detections of CO_2. Dubious and/or marginal detections of CO are marked as CO_2 + CO*, and are represented in gray.

The detection of CO_2 and CO across the distinct dynamical groups and spectral classifications of NPA23 are shown in Fig. 2. Notably, but unsurprisingly, CO was not detected in the Centaur population. However, CO was found to be predominantly in the Detached and Cold Classical populations, which only contain Double-Dip and Cliff objects. The Hot Classical population also showed a predominance of objects with both CO_2 and CO features, with the exception of two Bowl-type objects. In the Resonant and Scattering Disk populations, a more balanced mix of objects was found, with the detection of CO in five objects considered to be dubious or marginal (marked as CO_2 + CO* throughout the remainder of the manuscript).

The CO_2 fundamental bands were fit with a Gaussian to extract information about the band depth and center. We computed correlations between these parameters and visible slope, diameter, albedo, and perihelion distance. Fig 3 shows the distribution of these parameters, with the result of Pearson and Spearman correlation tests, and their statistical significance.

The upper left panel of Figure 3 shows a weak/moderate correlation between visible slope and CO_2 band depth. This suggests that objects with a redder color, which are also the ones with higher albedo (Fig. 3, *upper right*), may have a higher abundance of CO_2 compared to objects with a more neutral slope. Interestingly, all objects with a spectral slope higher than 18%/1000 Å are in the Double-Dip and Cliff groups and also exhibit a CO feature, except for 250112 (2002 KY_{14}), a Centaur with a perihelion distance of ~8.6 au, where CO is not stable against sublimation[31]. The deepest CO_2 features are seen on the Double-Dip group, where it is not correlated with the spectral slope when considering only the group itself. We hypothesize that the CO_2 fundamental feature in these spectra could be saturated, thus losing its linearity in the relation between band depth to the abundance of the ice.

The moderate to strong correlation between the CO_2 fundamental band depth and diameter, as well as perihelion distance, suggests that volatile-loss processes play a role in the abundance of CO_2 and CO on these objects. This correlation is stronger if only Double-Dip and Cliff groups are considered, since Bowl-n and Bowl appear to follow a different trend where a small content of CO_2 could be stable[32], or steadily produced[33], on their surfaces. The latter groups do not show any detectable CO feature and have more neutral visible slopes below 18%/1000 Å, and lower visible albedos (Fig. 3-*upper right*).

Figure 4 shows the perihelion temperature, where most of the volatile loss occurs, of each object along with the center positions of the fundamental band of CO_2. The objects with smaller CO_2 and no CO ice content (mostly Bowl and Bowl-n) display wide variations in temperatures up to 95 K while those with a high abundance of CO_2 and CO are very clustered in temperature, around 45 K. Notably, objects with only CO_2 have a wider dispersion of band centers, most of them shifted towards the longer wavelengths. In contrast, objects with CO_2 and CO (Cliff and Double-Dip) present a smaller variation in band centers, clustered in wavelengths between 4.25 - 4.27 μm. We compare these observations with laboratory spectra of CO_2 in different ice mixtures and for different temperatures as both parameters influence the band profile[34]. A fraction of

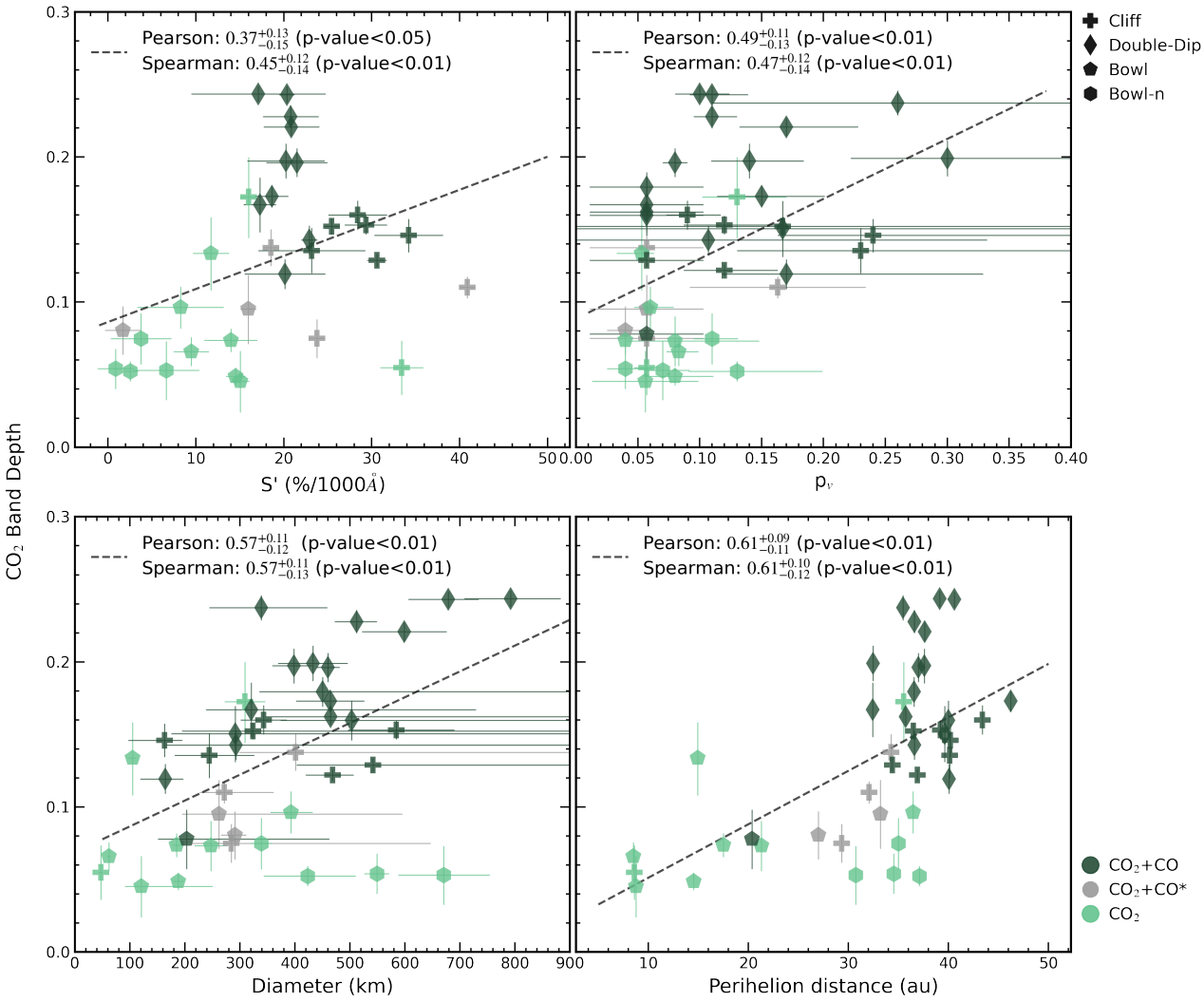

Figure 3. Distribution of CO_2 fundamental band depth for NPA23 spectral groups in relation to the visible slope (*upper left*), visible albedo (*upper right*), diameter (*lower left*), and perihelion distance (*lower right*). The Pearson and Spearman correlation coefficients for each test and their respective p-values are shown in each panel. Shapes denote NPA23 spectral groups, while colors encode CO_2 and CO presence.

Double-Dip and Cliff types The center position of several objects, mostly , fall in a region where CO_2 is pure or mixed with CO (shifts to shorter wavelengths). The remaining members of these groups (shifts to longer wavelengths), could be explained by mixtures with other polar molecules, such as $H_2O$and CH_3OH, which in different relative ratios explain the spread of observed values for the center position of the CO_2 fundamental band. Bowl and Bowl-n present a higher dispersion of values, with extreme values that are hard to explain. Nonetheless, the majority of members of these groups could be explained by mixtures with polar molecules.

The CO_2 fundamental band shape

The spectral shapes of the CO_2 fundamental band among the groups defined by NPA23 show a remarkable diversity, including the presence of wing-peaks surrounding the feature in some instances. To our knowledge, these structures have never been observed before for astronomical objects in or outside of the solar system. In order to reproduce the four types of CO_2 features, we utilized a light-scattering model for airless surfaces developed by Shkuratov et al. (1999)[35]. Our fits only consider the 4.1-4.5 μm region, where the CO_2 fundamental feature is located, and do not reproduce the full spectra. Therefore, the abundance ratios presented here are only relative estimates of abundance of the materials that were considered (CO_2, H_2O, CH_3OH, and others).

Fig. 5 shows the spectra of the best-fit models of the average spectrum of each spectral group. The CO_2 features on Bowl and Bowl-n groups were fit by intimate mixtures dominated by water ice with a minor component of CO_2 with sub-wavelength grain sizes. In contrast, CO_2, also with sub-wavelength grain sizes, is the dominant component for Double-Dip and Cliff groups, which is in agreement with their larger values of the fundamental band depth, and the presence of overtones.

Both Double-Dip and Cliff groups required more CO_2 and CH_3OH ice compared to the Bowl and Bowl-n groups. The higher abundance of CO_2 provided good fits to the $^{13}CO_2$ features, and both enhancements bordering the fundamental feature required the presence of $CH_3OH$to be reproduced. The Double-Dip model 2 shows that a higher content of methanol may "increase" the strength of the wing-peak at $\lambda < 4.27\mu$m. In the future, the use of more sophisticated models or consideration of other species (or mixtures of varying grain sizes of CO_2) could help reduce the differences between the models and the spectra of Double-Dip objects.

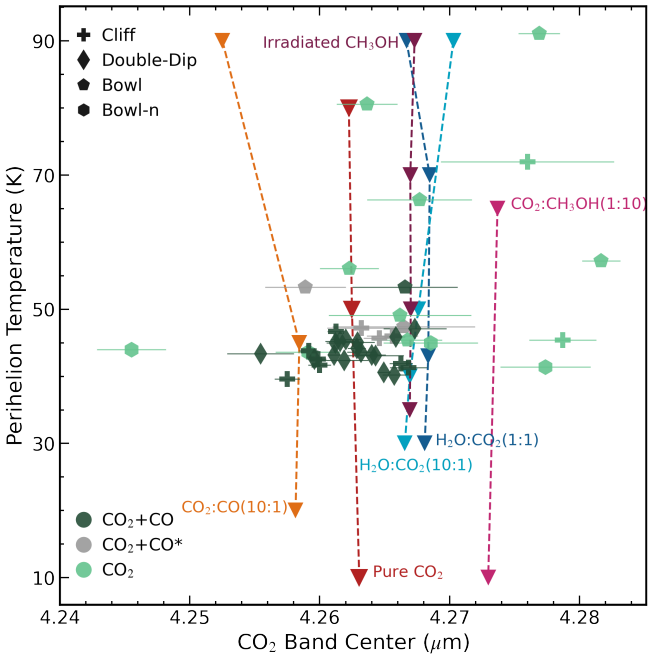

Figure 4. Observed fundamental CO_2 band center positions plotted against perihelion temperature, with comparisons to laboratory measurements of various ice mixtures at various temperatures (inverted triangles). TNOs shapes denote NPA23 spectral groups, while colors encode CO_2 and CO presence. Dashed lines connect the spectra of a mixture taken at different temperatures in the laboratory.

Discussion

We report the detection of CO_2 and CO in 42 and 24 TNOs, respectively, out of a sample of 45 objects observed with NIRSpec instrument on the JWST. CO_2 is widespread in the trans-Neptunian region, independent of the dynamical class. CO is also widespread and is a common constituent of the reddest and highest-albedo objects in our sample. Significant diversity of CO_2 and CO content are found in the sample. Our analysis suggests the prevalence of two distinct compositional classes of TNOs:

- Bowl and Bowl-n objects, which have high water ice content with small amounts of CO_2 ice and possible trace amounts of CO in a few of them (hereafter collectively referred to as BB).
- Cliff and Double-Dip objects, where CO_2 is a predominant ice, with varying amounts of CH_3OH and CO ices, and smaller amounts of water ice (hereafter referred to collectively as CD).

The existence of two major classes on TNOs has been extensively discussed in the literature, based on their color and other physical and dynamical properties[36–41]. However, limited information about their compositions was available to confirm or reject this hypothesis. As seen in Fig. 3, BB are gray while CD are redder, thus showing a clear compositional link to the historical color groups. Laboratory spectra (Fig. 4) show that the center position of the CO_2 fundamental absorption band in CD could be explained by CO_2 either segregated or dominant in mixtures with other molecules. In contrast, mixtures with H_2O are the preferred case for BB, even though the feature is highly shifted in several objects. Shifted values for the CO_2 band centers were also observed in icy moons of the giant planets, where mixes with polar mixtures have also been proposed[23], though they do not reproduce the full dispersion of centers measured for our sample and are in a different temperature regime that the one affecting the trans-Neptunian population.

A striking characteristic of the CO_2 observed in the TNOs is the unusual shape of the fundamental band, accompanied by the $^{13}CO_2$ feature and a broad absorption at 4.1 μm, all of these features are more evident in the CO_2-rich, CD group. BB objects have much less CO_2 and a 'normal' fundamental band profile. These characteristics can be approximately reproduced by models of intimate mixtures of water, methanol, and sub-wavelength particles of CO_2. We note that some of the difference between the CO_2 band shape between the Cliffs and Double-Dips may be due to the strong 4.1 μm absorption in the latter. The need for sub-wavelength particles and the difficulty in mimicking the shape of the wing-peaks for the Double-Dip group can also be taken as an indication that the physical state of the CO_2 might require more sophisticated models to reproduce the spectra. Nonetheless, the relative ratios of water, CO_2 , and methanol, based on the models of the CO_2 fundamental band, suggest a strong link, accretionary and/or evolutionary, between the CO_2 and intermediary molecules that control the spectral

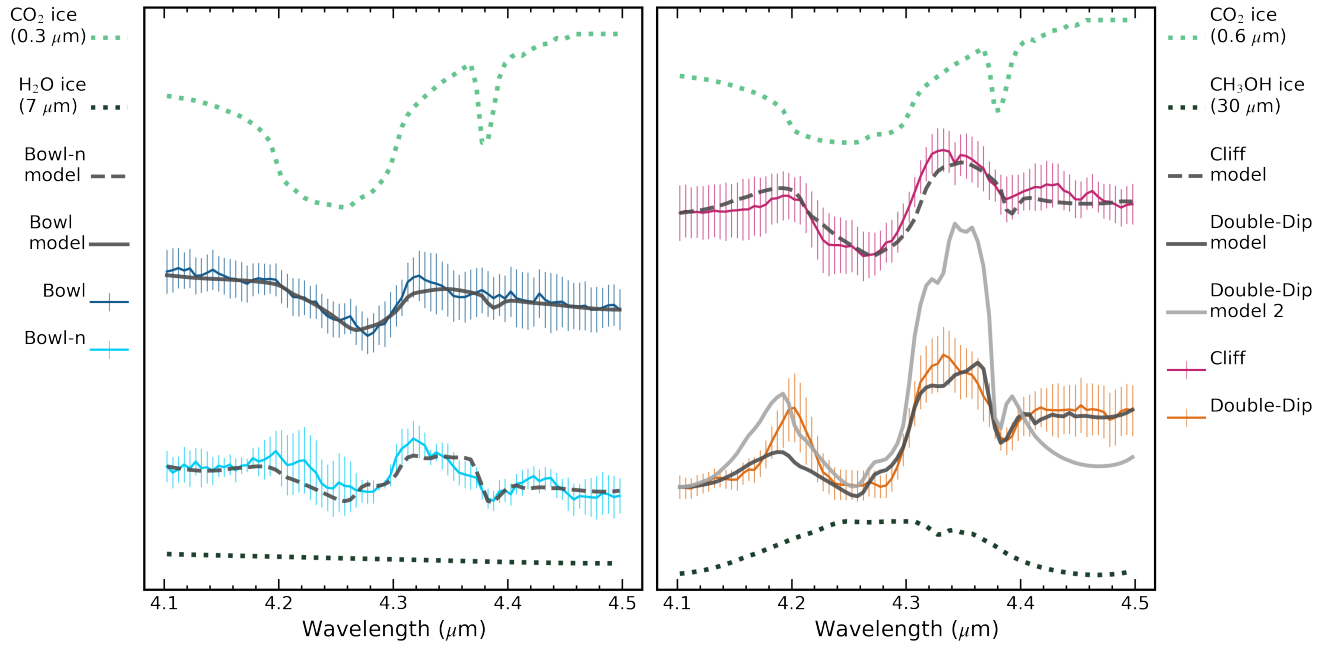

Figure 5. Intimate mixture models for the CO_2 fundamental band in each group defined by NPA23. The spectra of CO_2, H_2O, and CH_3OH pure ices are also shown as dotted lines. The *y*-axis is the normalized reflectances arbitrarily shifted for better visualization. The contrast in reflectance between the *left*- and *right*-panels are in different scales, therefore band depths should not be compared. Error bars represent the standard deviation within a group.

shape near 3 μm. Another remarkable aspect is the variation in the apparent abundance of 13CO2 between the groups, with the Double-Dip having significantly more. Fractionation by sublimation and escape would only very weakly favor retention of $^{13}CO_2$ over CO_2 (the mass ratio being 1.02), so perhaps the differences reflect condensation/accretion processes.

The different states and abundances of the CO_2 , CO, H_2O, and CH_3OH in the BB and CD groups, can not be explained by volatile retention mechanisms, which are dominated by the object size and equilibrium temperature, and suggest that these groups originated from separate regions of the solar system. Dynamical models for the formation and evolution of the early solar system propose that TNOs were formed within 20 to ∼50 au, beyond the frost lines of H_2O, CO_2, CH_3OH, and NH_3[42–44]. In the late migration scenario[36,43,44], objects would have remained in that region for several Myrs after the gas and dust of the disk dispersed, subjecting them to higher temperatures and triggering volatile loss during their post-accretional phase. Subsequent planetary migration would later place them in the current, and colder, trans-Neptunian region, where the remaining volatiles could be maintained, and changes in their surface properties by ion irradiation processes became stronger[1,6,36,45].

The BB and CD groups provide us with a picture of the post-accretional and evolutionary processes that ruled the construction of the trans-Neptunian region. A plausible scenario that could explain our observations is that BB objects formed in an inner icy region of the disk where the most volatile species were quickly depleted due to increased solar flux, resulting in the dominance of H_2O ice and smaller amounts of CO_2, which could be co-condensed with H_2O. The lower abundance of C-bearing species would prevent the formation of complex organics as reddening agents, which would result in them presenting more neutral colors. Several of these objects also show small perihelion distances when compared to the whole sample, so sublimation-driven loss of CO_2 could be contributing to their lower abundances of the ice. In contrast, CD objects could have formed further out, where CH_3OH, CO_2, and other C-bearing species were more abundant or could survive longer. The CO_2 in these objects could be mostly pure or co-condensed with other ices. A relation between diameter and CO_2 band depth is present only for the CD group, and not the BB, suggesting that variations of the abundance of this ice within the former is probably also determined by volatile-loss mechanisms, which could have operated more strongly in the early solar system, where objects would be closer to Sun.

CO ice has been previously reported in Pluto and is believed to be supported by the dwarf-planet's atmosphere via vapor pressure equilibrium and seasonal cycle activity[46,47]. The presence of a highly volatile ice, such as CO, in the CD objects as diverse in size as 138537 (2000 OK_{67}) and 174567 (2003 MW_{12}), with diameters of ∼164 km and ∼ 792 km, respectively, cannot be explained by models of the retention of primordial ices[1]. It is likely that CO was produced by irradiation of the dominant CO_2[48,49] or other C-bearing species like CH_3OH[8] and trapped in the surrounding less volatile ice. Irradiation of

these species, when mixed with H_2O ice, could also form complex organics, which may explain the redder spectral slope of these objects[8,50]. Additionally, a small amount of CO_2 may also have been produced by irradiation, summing up to the original inventory of CO2 in the body .

Future research should explore the complete compositional properties of these groups with more complex models, and investigate the effects of volatile loss and ion irradiation mechanisms on the balance between the destruction and preservation of icy content in these bodies. These studies, combined with the completion of the acquisition of DiSCo data, will allow a better comprehension of the early and late conditions that these objects experienced since their formation and the regions of the protoplanetary disk where they were formed.

Methods

The NPA23 Compositional Groups

The work of NPA23 provides a comprehensive overview of the DiSCo spectral collection, taken with JWST NIRSpec using the Prism/CLEAR combination. NPA23 includes detailed information about the reduction process, as well as a comprehensive list of ice absorption features that have been detected within the sample. An important aspect of that work is the clustering technique applied to the full spectral coverage of 42 TNOs and Centaurs. A combination of Principal Component Analysis and Spectral Clustering algorithms were used to identify four predominant groups of objects, which are studied here in terms of their CO_2 and CO content. These groups were named based on the structure of the 3-μm region (see Fig. 1: Bowl and Bowl-n are marked with a strong "bowl-shaped" absorption at $\sim$3 μm, including a Fresnel's peak at $\sim 3.15\mu$m, and absorption features at ~ 1.5 and $\sim 2.0\,\mu$m, all associated with the presence of water-ice; in contrast, Cliffs and Double-Dip are marked with a steep drop in reflectance after $\sim 2.5\mu$m, with a much weaker peak at $\sim 3.8\mu$m (stronger for Double-Dips), which is shifted to longer wavelengths in comparison to Bowl and Bowl-n, and the absence of the Fresnel's peak at these wavelength regions.

CO_2 Band Parameters

We applied a Gaussian fitting technique to the CO_2 fundamental band to extract parametric information, such as band center position and depth. Initially, the spectra of each target were normalized to unity using the median value of the wavelength range between 1.15 - 1.2 μm. The normalized reflectance was then transformed to a -log scale as a function of wavenumbers since the band profile is more symmetric in energy. We defined a local linear baseline between 4.20 and 4.33 µm for the continuum based on visual inspection. Note that in Cliff and Double-Dip spectra, the region for the continuum coincides with the wing-peaks surrounding the CO_2 fundamental feature. Once the continuum was removed, we fitted a single Gaussian curve on the band and extracted their amplitudes and peak positions. These values were then transformed back to wavelength and linear scale to represent the band center position and depth. To estimate the uncertainties of these parameters, we resampled the spectra using a Gaussian distribution for each spectral point, where the normalized reflectance nominal value was considered as the mean, and the uncertainty as the standard deviation. The resampled points were randomly drawn from these Gaussians and used to recalculate the band parameters with the aforementioned procedure. This step was repeated for a thousand iterations, producing a distribution of values for each spectrum. Finally, the average and standard deviation of the parameters over all iterations were taken as the nominal values and uncertainties for the CO_2 fundamental band center and depth. Table 1 shows the results of this analysis, coupled with the detection of CO signatures based on visual inspection.

We investigated possible correlations of CO_2 band parameters with various targets' physical and dynamical properties, including diameter, albedo, visible slope, perihelion distance, and perihelion temperature. Table 2 lists these parameters for the DiSCo sample used in this work. The visible spectral slopes were extracted from multiple works in the literature[38–40,51], when spectrum was not available, the photometric fluxes in similar wavelengths were used to estimate the slope. This parameter, named S', measures the inclination of the spectra at visible wavelengths ($\sim 0.5-0.9\mu$m) and is given in $\%/1000$Å. Diameter and albedos were extracted from the "TNOs are Cool" project[52–59]. For objects that did not have any albedo measurement in the literature, the average albedo of their dynamical classes was taken and used to estimate the diameter[60]. Finally, albedo values, combined with phase integral also extracted from the literature[61,62], were used to estimate the Bond albedo and to determine the perihelion temperature for each object.

The two most commonly used correlation tests are the Pearson correlation test and the Spearman correlation test. The Pearson correlation test measures the linear relationship between two continuous variables while the Spearman correlation test measures the monotonic relationship between two variables based on their ranks. Pearson is sensitive to linear relationships while Spearman is more sensitive to non-linear relationships. Both coefficients can range from -1 to 1, where negative numbers indicate an anti-correlation. A weak correlation is generally considered to be a value between 0.1 and 0.3, a moderate correlation is between 0.3 and 0.5, and a strong correlation is above 0.5. The error bars for these correlations were estimated following[63] The results of these tests, including their statistical significance and interpretation are described throughout the manuscript.

To compare the CO_2 fundamental band center positions with laboratory data, we interpolated the latter to NIRSpec spectral resolution and fitted it with a single Gaussian as well. We stress that this fitting method is not meant to be representative of

the true molecular complexity, since band profile can get very complex, but rather to highlight a global trend in the shift of the band of CO_2 for different mixtures. Laboratory data of pure and mixed CO_2 were gathered from the LIDA database[64]. Ice mixtures were prepared at low temperatures and then heated to the temperatures selected here to represent the variability between aphelion and perihelion temperatures. We investigated pure CO_2 ice[65], CO_2 with CO as a minor component[66] and

Number	Name	Prov. Des.	Group	CO_2 Center (μm)	CO_2 Depth (%)	CO
-	-	2012 DR30	Bowl	4.282 ± 0.001	$4.874^{+0.602}_{-0.606}$	No
32532	Thereus	2001 PT13	Bowl	4.264 ± 0.002	$6.594^{+0.977}_{-0.988}$	No
35671	-	1998 SN165	Bowl	4.267 ± 0.003	$9.637^{+1.438}_{-1.461}$	No
42355	Typhon	2002 CR46	Bowl	4.262 ± 0.002	$7.367^{+0.809}_{-0.817}$	No
120216	-	2004 EW95	Bowl	4.259 ± 0.003	$8.057^{+1.642}_{-1.672}$	Maybe
136204	-	2003 WL7	Bowl	4.268 ± 0.004	$13.363^{+2.480}_{-2.553}$	No
309239	-	2007 RW10	Bowl	4.266 ± 0.005	$7.319^{+1.706}_{-1.738}$	No
468861	-	2013 LU28	Bowl	4.277 ± 0.002	$4.533^{+2.088}_{-2.135}$	No
508338	-	2015 SO20	Bowl	4.266 ± 0.005	$9.522^{+2.336}_{-2.398}$	Maybe
545293	-	2005 CC79	Bowl	4.267 ± 0.004	$7.791^{+2.022}_{-2.068}$	Yes
15874	-	1996 TL66	Bowl-n	4.246 ± 0.003	$7.485^{+1.745}_{-1.778}$	No
444030	-	2004 NT33	Bowl-n	4.259 ± 0.002	$5.239^{+0.688}_{-0.693}$	No
455502	-	2003 UZ413	Bowl-n	4.277 ± 0.003	$5.298^{+1.999}_{-2.042}$	No
612533	-	2002 XV93	Bowl-n	4.269 ± 0.004	$5.402^{+1.368}_{-1.388}$	No
48639	-	1995 TL8	Cliff	4.258 ± 0.001	$13.558^{+1.541}_{-1.569}$	Yes
66652	Borasisi	1999 RZ253	Cliff	4.267 ± 0.001	$14.596^{+1.138}_{-1.153}$	Yes
79360	Sila-Nunam	1997 CS29	Cliff	4.266 ± 0.001	$16.002^{+0.995}_{-1.007}$	Yes
84522	-	2002 TC302	Cliff	4.260 ± 0.001	$15.314^{+0.645}_{-0.649}$	Yes
175113	-	2004 PF115	Cliff	4.260 ± 0.001	$12.196^{+0.396}_{-0.398}$	Yes
250112	-	2002 KY14	Cliff	4.276 ± 0.007	$5.490^{+1.855}_{-1.892}$	No
307982	-	2004 PG115	Cliff	4.259 ± 0.001	$15.226^{+0.556}_{-0.559}$	Yes
444745	-	2007 JF43	Cliff	4.265 ± 0.001	$11.009^{+0.752}_{-0.759}$	Maybe
445473	-	2010 VZ98	Cliff	4.261 ± 0.001	$12.883^{+0.461}_{-0.464}$	Yes
469750	-	2005 PU21	Cliff	4.263 ± 0.003	$7.494^{+1.328}_{-1.347}$	Maybe
470316	-	2007 OC10	Cliff	4.279 ± 0.003	$17.249^{+2.734}_{-2.827}$	No
523722	-	2014 LV28	Cliff	4.266 ± 0.002	$13.763^{+1.255}_{-1.274}$	Maybe
82155	-	2001 FZ173	Double-Dip	4.267 ± 0.002	$16.714^{+1.855}_{-1.898}$	Yes
120132	-	2003 FY128	Double-Dip	4.264 ± 0.001	$19.618^{+0.987}_{-0.999}$	Yes
120348	-	2004 TY364	Double-Dip	4.263 ± 0.001	$22.781^{+0.784}_{-0.792}$	Yes
138537	-	2000 OK67	Double-Dip	4.264 ± 0.002	$11.936^{+1.016}_{-1.028}$	Yes
144897	-	2004 UX10	Double-Dip	4.263 ± 0.001	$19.730^{+1.184}_{-1.202}$	Yes
145452	-	2005 RN43	Double-Dip	4.261 ± 0.000	$24.303^{+0.569}_{-0.574}$	Yes
145480	-	2005 TB190	Double-Dip	4.266 ± 0.001	$17.294^{+0.692}_{-0.698}$	Yes
174567	Varda	2003 MW12	Double-Dip	4.265 ± 0.000	$24.358^{+0.548}_{-0.552}$	Yes
229762	G!kun||homdima	2007 UK126	Double-Dip	4.260 ± 0.001	$22.073^{+0.626}_{-0.631}$	Yes
230965	-	2004 XA192	Double-Dip	4.261 ± 0.001	$23.732^{+0.851}_{-0.860}$	Yes
470596	-	2008 NW4	Double-Dip	4.262 ± 0.001	$14.280^{+1.002}_{-1.014}$	Yes
471137	-	2010 ET65	Double-Dip	4.255 ± 0.003	$15.054^{+1.905}_{-1.949}$	Yes
471143	Dziewanna	2010 EK139	Double-Dip	4.263 ± 0.001	$19.909^{+1.216}_{-1.234}$	Yes
471210	-	2010 VW11	Double-Dip	4.262 ± 0.001	$17.940^{+1.007}_{-1.019}$	Yes
523777	-	2014 YF50	Double-Dip	4.266 ± 0.001	$16.222^{+0.580}_{-0.584}$	Yes
552555	-	2010 ER65	Double-Dip	4.262 ± 0.002	$15.974^{+1.359}_{-1.382}$	Yes
52872	Okyrhoe	1998 SG35	Misfit	-	-	No
310071	-	2010 KR59	Misfit	-	-	No
416400	-	2003 UZ117	Misfit	-	-	No

Table 1. Results of the CO_2 fundamental band parameter extracted using Gaussian fitting. Detections of CO based on visual inspection are also listed.

Number	Name	Prov Des	DC	a (au)	e	i (°)	q (au)	H (mag)	D (km)	p_V	H/E	T_q (K)	S' vis (%/1000Å)
32532	Thereus	2001 PT13	Centaur	10.6	0.20	20.4	8.5	9.2	62^{+3}_{-3}	$0.08^{+0.02}_{-0.01}$	S/H	95	9.48±2.01
52872	Okyrhoe	1998 SG35	Centaur	8.4	0.30	15.6	5.8	10.9	35^{+3}_{-3}	$0.06^{+0.01}_{-0.01}$	S/H	115	11.27±3.22
136204	-	2003 WL7	Centaur	20.1	0.26	11.2	14.9	8.7	105^{+6}_{-7}	$0.05^{+0.01}_{-0.02}$	S/H	72	11.7±2.06
250112	-	2002 KY14	Centaur	12.6	0.32	19.5	8.6	9.7	47^{+3}_{-4}	$0.06^{+0.01}_{-0.01}$	S/H	94	33.42±2.46
310071	-	2010 KR59	Centaur	29.8	0.56	19.7	13.0	7.8	110^{+30}_{-30}	$0.12^{+0.04}_{-0.04}$	S/H	76	23.89±4.47
468861	-	2013 LU28	Centaur	190.8	0.95	125.3	8.7	8.3	120^{+130}_{-30}	$0.06^{+0.04}_{-0.04}$	E	94	15.06±1.0
-	-	2012 DR30	Centaur	1003.8	0.99	78.0	14.5	7.1	188^{+9}_{-9}	$0.08^{+0.03}_{-0.03}$	S/H	72	14.5±1.1
15874	-	1996 TL66	Scattering	84.3	0.59	23.9	35.0	5.4	339^{+20}_{-20}	$0.11^{+0.02}_{-0.02}$	S/H	46	3.75±3.46
42355	Typhon	2002 CR46	Scattering	37.5	0.53	2.4	17.5	7.6	185^{+7}_{-7}	$0.04^{+0.01}_{-0.01}$	S/H	66	13.97±3.01
82155	-	2001 FZ173	Scattering	84.3	0.62	12.7	32.4	6.2	320^{+408}_{-82}	$0.06^{+0.05}_{-0.05}$	E	48	17.27±1.84
309239	-	2007 RW10	Scattering	30.4	0.30	36.0	21.3	6.8	247^{+30}_{-30}	$0.08^{+0.07}_{-0.04}$	S/H	60	-
445473	-	2010 VZ98	Scattering	158.3	0.78	4.5	34.4	5.1	541^{+691}_{-138}	$0.06^{+0.05}_{-0.05}$	E	47	30.59±1.12
469750	-	2005 PU21	Scattering	184.0	0.84	6.2	29.3	6.5	284^{+362}_{-72}	$0.06^{+0.05}_{-0.05}$	E	51	23.75±0.9
471210	-	2010 VW11	Scattering	51.0	0.28	27.8	36.6	5.5	450^{+574}_{-115}	$0.06^{+0.05}_{-0.05}$	E	45	-
508338	-	2015 SO20	Scattering	172.7	0.81	23.4	33.2	6.6	261^{+333}_{-67}	$0.06^{+0.05}_{-0.05}$	E	48	15.95±0.9
523722	-	2014 LV28	Scattering	70.0	0.51	10.7	34.3	5.7	401^{+512}_{-102}	$0.06^{+0.05}_{-0.05}$	E	47	18.54±0.9
523777	-	2014 YF50	Scattering	78.9	0.55	18.2	35.7	5.4	465^{+593}_{-119}	$0.06^{+0.05}_{-0.05}$	E	46	-
545293	-	2005 CC79	Scattering	47.5	0.57	18.3	20.4	7.2	203^{+259}_{-52}	$0.06^{+0.05}_{-0.05}$	E	61	-
552555	-	2010 ER65	Scattering	96.7	0.59	21.3	40.0	5.2	503^{+642}_{-128}	$0.06^{+0.05}_{-0.05}$	E	43	-
84522	-	2002 TC302	Resonant	55.6	0.30	35.0	39.2	3.9	584^{+105}_{-88}	$0.12^{+0.05}_{-0.03}$	S/H	44	29.33±2.4
120216	-	2004 EW95	Resonant	39.3	0.31	29.3	27.0	6.6	291^{+20}_{-25}	$0.04^{+0.02}_{-0.02}$	S/H	53	1.71±2.06
444745	-	2007JF43	Resonant	39.3	0.19	15.1	32.0	5.4	271^{+89}_{-44}	$0.16^{+0.07}_{-0.07}$	E	49	40.89±0.9
455502	-	2003 UZ413	Resonant	39.4	0.22	12.0	30.7	4.3	670^{+84}_{-82}	$0.07^{+0.02}_{-0.02}$	S/H	50	6.64±3.72
471143	Dziewanna	2010 EK139	Resonant	69.1	0.53	29.5	32.5	4.1	433^{+63}_{-64}	$0.30^{+0.11}_{-0.08}$	S/H	47	-
612533	-	2002 XV93	Resonant	39.3	0.12	13.3	34.5	4.9	549^{+21}_{-23}	$0.04^{+0.02}_{-0.02}$	S/H	47	0.85±2.06
35671	-	1998 SN165	Hot Classical	38.2	0.05	4.6	36.5	5.7	393^{+39}_{-38}	$0.06^{+0.02}_{-0.01}$	S/H	46	8.24±4.91
120348	-	2004 TY364	Hot Classical	39.1	0.06	24.8	36.6	4.4	512^{+37}_{-40}	$0.11^{+0.02}_{-0.02}$	S/H	46	20.78±3.17
138537	-	2000 OK67	Hot Classical	47.0	0.15	4.9	40.0	6.2	164^{+33}_{-45}	$0.17^{+0.16}_{-0.05}$	S/H	43	20.14±4.59
144897	-	2004 UX10	Hot Classical	39.3	0.04	9.5	37.6	4.4	398^{+32}_{-39}	$0.14^{+0.04}_{-0.03}$	S/H	45	20.23±4.4
145452	-	2005 RN43	Hot Classical	41.9	0.03	19.2	40.6	3.7	679^{+55}_{-73}	$0.11^{+0.03}_{-0.02}$	S/H	43	20.34±0.9
174567	Varda	2003 MW12	Hot Classical	45.8	0.15	21.5	39.1	3.5	792^{+91}_{-84}	$0.10^{+0.02}_{-0.02}$	S/H	44	17.11±7.64
175113	-	2004 PF115	Hot Classical	39.3	0.06	13.4	36.9	4.5	468^{+38}_{-49}	$0.12^{+0.04}_{-0.03}$	S/H	45	-
416400	-	2003 UZ117	Hot Classical	44.4	0.14	27.4	38.4	5.3	222^{+57}_{-42}	$0.29^{+0.16}_{-0.11}$	S/H	43	-2.1±2.0
444030	-	2004 NT33	Hot Classical	43.8	0.15	31.2	37.1	4.6	423^{+87}_{-80}	$0.13^{+0.07}_{-0.04}$	S/H	45	2.54±0.9
470596	-	2008 NW4	Hot Classical	45.6	0.20	23.1	36.6	5.7	293^{+665}_{-127}	$0.11^{+0.22}_{-0.22}$	E	46	22.89±0.9
66652	Borasisi	1999 RZ253	Cold Classical	44.1	0.09	0.6	40.2	5.9	163^{+32}_{-66}	$0.24^{+0.44}_{-0.08}$	S/H	42	34.2±3.9
79360	Sila-Nunam	1997 CS29	Cold Classical	43.7	0.01	2.3	43.4	5.3	343^{+42}_{-42}	$0.09^{+0.03}_{-0.02}$	S/H	42	28.39±3.34
48639	-	1995 TL8	Detached	53.0	0.24	0.2	40.1	4.9	244^{+82}_{-63}	$0.23^{+0.19}_{-0.10}$	S/H	43	23.17±6.08
120132	-	2003 FY128	Detached	49.1	0.25	11.8	37.0	4.8	460^{+21}_{-21}	$0.08^{+0.01}_{-0.01}$	S/H	45	21.48±3.46
145480	-	2005 TB190	Detached	76.9	0.40	26.4	46.2	4.5	464^{+62}_{-62}	$0.15^{+0.05}_{-0.04}$	S/H	40	18.63±1.89
229762	G!kun||homdima	2007 UK126	Detached	73.9	0.49	23.4	37.6	3.5	599^{+77}_{-77}	$0.17^{+0.06}_{-0.04}$	S/H	44	20.85±3.17
230965	-	2004 XA192	Detached	47.2	0.25	38.2	35.5	4.3	339^{+120}_{-95}	$0.26^{+0.34}_{-0.15}$	S/H	45	-
307982	-	2004 PG115	Detached	92.1	0.60	16.3	36.5	5.0	323^{+999}_{-128}	$0.17^{+0.29}_{-0.29}$	E	46	25.42±0.9
470316	-	2007 OC10	Detached	50.2	0.29	21.7	35.5	5.3	$309\$^{+37}_{-37}$	$0.13^{+0.04}_{-0.03}$	S/H	46	16.0±0.9
471137	-	2010 ET65	Detached	61.7	0.36	30.7	39.6	5.2	291^{+898}_{-115}	$0.17^{+0.29}_{-0.29}$	E	44	-

Table 2. Dynamical and physical properties of DiSCo targets analyzed in this work. The column H/E marks if the diameters were taken from Spitzer/Hershel observations (S/H), or estimated (E) based on the average albedo of the dynamical class.

CO_2 mixed with or in polar ice like H_2O and CH_3OH[34]. We also included CO_2 formed by irradiation of CH_3OH for which a H_2O:CH_3OH (1:1) ice mixture was prepared and irradiated with 30 keV H^+ at 35K and then heated[50]. Interpolation and Gaussian fits were performed using Quasar's spectroscopy toolbox[67].

CO_2 fundamental band models

We used a Bayesian inference framework to find local fits to the CO_2 fundamental feature for the spectra of each individual group from NPA23. We stress that the focus here is not to model the whole spectra of the groups, but rather to investigate the mechanisms that could be producing the unexpected profile of the absorption features. The average spectrum of each group was first trimmed from 4.1 μm to 4.5 μm to select only the spectral region containing the CO_2 fundamental feature (Fig. 1).

Bayesian inference requires a forward model that could produce synthetic spectra comparable to those observed by JWST. Here we use the simplified one-dimensional geometrical-optics formulation by Shkuratov et al. (1999)[35] for the scattering of light on particulate surfaces as the forward model. The model estimates the interaction of incident light with a medium of regolith grains by approximating the surface with a thick slab, where the radiation undergoes multiple scattering events and becomes diffuse within the medium. As a result, the direction of the radiation becomes randomized, and the radiation is assumed to be emitted and absorbed isotropically within the medium. We caution that this assumption may not hold true for sub-wavelength grains, and the sense of grain might lose its meaning. The input for the model includes the grain size, abundance, and porosity, which define the prior parameter space that needs to be explored. The porosity has minor effects on the overall shape of the spectra and was fixed at 0.5.

In the context of Bayesian statistics, we are interested in finding the posterior distribution $P(\Theta|D,M)$ of a set of input parameters Θ (fractions, grain sizes, and porosity) for the model (M) that best-fit the spectroscopic data (D), obtained by a telescope. To estimate the posterior, we refer to the Bayes theorem:

$$P(\Theta|D,M) = \frac{L(D|\Theta,M)\pi(\Theta|M)}{Z(D|M)} \tag{1}$$

where $L(D|\Theta,M)$ is the likelihood of the observed spectra given the input parameters for the model, $\pi(\Theta,M)$ is the prior knowledge about these input parameters, and $Z(D,M)$ is the evidence, which is the integral of the model over the all prior domain Ω_Θ (i.e. over all possible combinations of parameters):

$$Z(D|M) = \int_{\Omega_\Theta} L(D|\Theta,M)\pi(\Theta,M)d\Theta \tag{2}$$

The dimension of this integral is equal to the number of parameters of the model, i.e., twice (grain sizes and fractional abundances) the number of optical constants used. This number can be significantly high if the surface of the object is constituted of a mixture of several materials with different grain size distributions. Therefore, the computation of the evidence can be challenging, and analytically intractable, requiring the use of numerical methods. We used the `dynesty`[68,69] Python-language implementation of Nested Sampling[70,71] for this task, which allows an efficient sample of high-dimensional parameter space by repetitively shrinking the prior domain based on likelihood constraints, towards maximizing the likelihood. The algorithm maintains a set of "live" points (n_{live}) to occupy the posterior distribution. At each iteration, random points are sampled from the prior domain (Ω_θ), and their likelihoods are calculated. The points with the lowest likelihoods are used to define an iso-likelihood contour and are sequentially discarded. This iso-likelihood is used as a hard constraint to the sampling of new points, and this procedure is repeated until convergence, or in the nested sampling case until the desired resolution for the evidence calculation, is obtained.

A required condition for generating spectra of internally mixed materials is that their fractional abundances sum to unity. This criterion can be fulfilled by using a Dirichlet distribution for the prior fractional abundance. The Dirichlet probability density function (PDF) is given by:

$$\pi(\Theta,M) = Dir(x_1,x_2,...;\alpha_1,\alpha_2,...) = \frac{1}{B(\alpha)}\prod_{i=1}^{K} x^{\alpha_i-1} \tag{3}$$

with x representing the abundance of a component, α is the concentration parameter, and $B(\alpha)$ is the multinomial beta function:

$$B(\alpha) = \frac{\prod_{i=1}^{K}\Gamma(\alpha_i)}{\Gamma(\sum_{i=1}^{K}\alpha_i)}, \tag{4}$$

where Γ is the gamma function. The α parameter measures the uniformity of the distribution. If $\alpha_i = 1$ for each component, the PDF of all components is even, and therefore all components are sampled uniformly.

In contrast to the fractional abundance prior, the grain sizes can assume any value within a boundary. Therefore, in this case, we use a Uniform distribution:

$$U(g) = \begin{cases} \frac{1}{g_{max} - g_{min}} & \text{for } g_{min} \leq g \leq g_{max} \\ 0 & \text{for } g_{min} < g \text{ and } g_{max} > g \end{cases} \quad (5)$$

In this work, we allowed the grain sizes to vary between 0.1 to 1000 μm (g_{min} and g_{max}). The nested sampling technique requires that the prior distribution for both the fractional abundances and grain sizes are transformed into hypercube units, where dimensions have lengths equal to unity.

Finally, the likelihood is estimated by the chi-square "distance" between the observed spectra (D) and the one produced for an intimate mixture with the model (M) with a set of input parameters Θ_i.

$$L(\Theta|D,M) = -0.5 \times log(\chi^2) \quad (6)$$

where χ^2 is given by the general formula:

$$\chi^2 = \sum_{i=1}^{N} \frac{(D_i - M_i^{\Theta})^2}{\sigma_i^2} \quad (7)$$

where D_i and M_i^{Θ} are the normalized spectral reflectance at the i-th wavelength of the observed and synthetic data, respectively.

The optical constants that were used for the modeling include water-ice, organics, methanol, CO_2, complex organics, and silicates. Detailed information about these optical constants and their references is presented in Table 3. Results for the best fit of the CO_2 fundamental feature of each group from NPA23 are presented in Table 4 and Fig. 5. We include an additional model for the Double-Dip (M2), which shows more prominent wing-peaks as a result of higher methanol abundance.

Optical Constant	Phase	Temperature	Ref
CO_2	-	12.5 K	[72]
H_2O	amorphous	40 K	[73,74]
H_2O	crystalline	40 K	[73,74]
CH_3OH	amorphous	100K	[75,76]
Titan tholin	-	170 K	[77]
Tritan tholin	-	170 K	[77]
Piroxene (P4)	-	-	[78]
Olivine	-	-	[78]

Table 3. Optical constants used for the models in this work.

Group	Water ice		CO_2		Methanol		Other components
	Abundance (%)	Grain size (μm)	Abundance (%)	Grain size (μm)	Abundance (%)	Grain size (μm)	Abundance (%)
Bowl	54.2	1	1	0.35	1.2	350	45.4
Bowl-N	77	6.5	1.3	0.6	7.4	300	14.3
Cliff	1	350	61	0.3	14	250	24
Double-Dip	< 1	-	59	0.6	31	250	9
Double-Dip M2	0	-	50	0.6	50	250	0

Table 4. Best-fit mixture models for local fitting of the CO_2 fundamental band. Other components include complex organics (Titan and Triton tholin), and silicates (Olivine and Piroxene).

References

1. Schaller, E. L. & Brown, M. E. Volatile Loss and Retention on Kuiper Belt Objects. *Astrophys. J. Lett.* **659**, L61–L64, DOI: 10.1086/516709 (2007).

2. Johnson, R. E., Oza, A., Young, L. A., Volkov, A. N. & Schmidt, C. Volatile Loss and Classification of Kuiper Belt Objects. *Astrophys. J.* **809**, 43, DOI: 10.1088/0004-637X/809/1/43 (2015). 1503.05315.

3. Young, L. A., Braga-Ribas, F. & Johnson, R. E. Volatile evolution and atmospheres of Trans-Neptunian objects. In Prialnik, D., Barucci, M. A. & Young, L. (eds.) *The Trans-Neptunian Solar System*, 127–151, DOI: 10.1016/B978-0-12-816490-7.00006-0 (Elsevier, 2020).

4. Fray, N. & Schmitt, B. Sublimation of ices of astrophysical interest: A bibliographic review. *Planet. Space Sci.* **57**, 2053–2080, DOI: 10.1016/j.pss.2009.09.011 (2009).

5. Strazzulla, G. & Johnson, R. E. Irradiation Effects on Comets and Cometary Debris. In Newburn, J., R. L., Neugebauer, M. & Rahe, J. (eds.) *IAU Colloq. 116: Comets in the post-Halley era*, vol. 167 of *Astrophysics and Space Science Library*, 243, DOI: 10.1007/978-94-011-3378-4_11 (1991).

6. Brunetto, R., Barucci, M. A., Dotto, E. & Strazzulla, G. Ion Irradiation of Frozen Methanol, Methane, and Benzene: Linking to the Colors of Centaurs and Trans-Neptunian Objects. *Astrophys. J.* **644**, 646–650, DOI: 10.1086/503359 (2006).

7. de Bergh, C., Schmitt, B., Moroz, L. V., Quirico, E. & Cruikshank, D. P. Laboratory Data on Ices, Refractory Carbonaceous Materials, and Minerals Relevant to Transneptunian Objects and Centaurs. In Barucci, M. A., Boehnhardt, H., Cruikshank, D. P., Morbidelli, A. & Dotson, R. (eds.) *The Solar System Beyond Neptune*, 483–506 (University of Arizona Press, 2008).

8. Quirico, E. *et al.* On a radiolytic origin of red organics at the surface of the Arrokoth Trans-Neptunian Object. *Icarus* **394**, 115396, DOI: 10.1016/j.icarus.2022.115396 (2023).

9. Barkume, K. M., Brown, M. E. & Schaller, E. L. Near-Infrared Spectra of Centaurs and Kuiper Belt Objects. *Astron. J.* **135**, 55–67, DOI: 10.1088/0004-6256/135/1/55 (2008).

10. Guilbert, A. *et al.* ESO-Large Program on TNOs: Near-infrared spectroscopy with SINFONI. *Icarus* **201**, 272–283, DOI: 10.1016/j.icarus.2008.12.023 (2009).

11. Barucci, M. A. *et al.* New insights on ices in Centaur and Transneptunian populations. *Icarus* **214**, 297–307, DOI: 10.1016/j.icarus.2011.04.019 (2011).

12. Cruikshank, D. P. *et al.* The Composition of Centaur 5145 Pholus. *Icarus* **135**, 389–407, DOI: 10.1006/icar.1998.5997 (1998).

13. Barucci, M. A., Merlin, F., Dotto, E., Doressoundiram, A. & de Bergh, C. TNO surface ices. Observations of the TNO 55638 (2002 VE_{95}) and analysis of the population's spectral properties. *Astron. Astrophys.* **455**, 725–730, DOI: 10.1051/0004-6361:20064951 (2006).

14. Stern, S. A. *et al.* Initial results from the New Horizons exploration of 2014 MU_{69}, a small Kuiper Belt object. *Science* **364**, aaw9771, DOI: 10.1126/science.aaw9771 (2019). 2004.01017.

15. Cook, J. C., Desch, S. J., Roush, T. L., Trujillo, C. A. & Geballe, T. R. Near-Infrared Spectroscopy of Charon: Possible Evidence for Cryovolcanism on Kuiper Belt Objects. *Astrophys. J.* **663**, 1406–1419, DOI: 10.1086/518222 (2007).

16. Cook, J. C. *et al.* Composition of Pluto's small satellites: Analysis of New Horizons spectral images. *Icarus* **315**, 30–45, DOI: 10.1016/j.icarus.2018.05.024 (2018).

17. Clark, R. N., Carlson, R., Grundy, W. & Noll, K. *Observed Ices in the Solar System*, 3–46 (Springer New York, New York, NY, 2013).

18. Rubanenko, L., Mazarico, E., Neumann, G. A. & Paige, D. A. Ice in Micro Cold Traps on Mercury: Implications for Age and Origin. *J. Geophys. Res. (Planets)* **123**, 2178–2191, DOI: 10.1029/2018JE005644 (2018).

19. Schorghofer, N., Williams, J.-P., Martinez-Camacho, J., Paige, D. A. & Siegler, M. A. Carbon Dioxide Cold Traps on the Moon. *Geophys. Res. Lett.* **48**, e95533, DOI: 10.1029/2021GL095533 (2021).

20. Phillips, R. J. *et al.* Massive CO_2 Ice Deposits Sequestered in the South Polar Layered Deposits of Mars. *Science* **332**, 838, DOI: 10.1126/science.1203091 (2011).

21. McCord, T. B. *et al.* Non-water-ice constituents in the surface material of the icy Galilean satellites from the Galileo near-infrared mapping spectrometer investigation. *J. Geophys. Res.* **103**, 8603–8626, DOI: 10.1029/98JE00788 (1998).

22. Grundy, W. M. *et al.* Distributions of H $_2$O and CO $_2$ ices on Ariel, Umbriel, Titania, and Oberon from IRTF/SpeX observations. *Icarus* **184**, 543–555, DOI: 10.1016/j.icarus.2006.04.016 (2006).

23. Cruikshank, D. P. *et al.* Carbon dioxide on the satellites of Saturn: Results from the Cassini VIMS investigation and revisions to the VIMS wavelength scale. *Icarus* **206**, 561–572, DOI: 10.1016/j.icarus.2009.07.012 (2010).

24. Pinilla-Alonso, N., Roush, T. L., Marzo, G. A., Cruikshank, D. P. & Dalle Ore, C. M. Iapetus surface variability revealed from statistical clustering of a VIMS mosaic: The distribution of CO $_2$. **215**, 75–82, DOI: 10.1016/j.icarus.2011.07.004 (2011).

25. Cartwright, R. J., Emery, J. P., Rivkin, A. S., Trilling, D. E. & Pinilla-Alonso, N. Distribution of CO_2 ice on the large moons of Uranus and evidence for compositional stratification of their near-surfaces. *Icarus* **257**, 428–456, DOI: 10.1016/j.icarus.2015.05.020 (2015). 1506.04673.

26. Harrington Pinto, O., Womack, M., Fernandez, Y. & Bauer, J. A Survey of CO, CO_2, and H_2O in Comets and Centaurs. **3**, 247, DOI: 10.3847/PSJ/ac960d (2022). 2209.09985.

27. Cruikshank, D. P. *et al.* Ices on the Surface of Triton. *Science* **261**, 742–745, DOI: 10.1126/science.261.5122.742 (1993).

28. Grundy, W. M. & Young, L. A. Near-infrared spectral monitoring of Triton with IRTF/SpeX I: establishing a baseline for rotational variability. *Icarus* **172**, 455–465, DOI: 10.1016/j.icarus.2004.07.013 (2004).

29. Agnor, C. B. & Hamilton, D. P. Neptune's capture of its moon Triton in a binary-planet gravitational encounter. *Nature* **441**, 192–194, DOI: 10.1038/nature04792 (2006).

30. Böker, T. *et al.* The Near-Infrared Spectrograph (NIRSpec) on the James Webb Space Telescope. III. Integral-field spectroscopy. *Astron. & Astrophys.* **661**, A82, DOI: 10.1051/0004-6361/202142589 (2022). 2202.03308.

31. Gkotsinas, A., Guilbert-Lepoutre, A., Raymond, S. N. & Nesvorny, D. Thermal Processing of Jupiter-family Comets during Their Chaotic Orbital Evolution. **928**, 43, DOI: 10.3847/1538-4357/ac54ac (2022). 2202.06685.

32. Collings, M. P. *et al.* A laboratory survey of the thermal desorption of astrophysically relevant molecules. *Mon. Notices Royal Astron. Soc.* **354**, 1133–1140 (2004).

33. Mennella, V., Baratta, G., Palumbo, M. & Bergin, E. Synthesis of co and co2 molecules by uv irradiation of water ice-covered hydrogenated carbon grains. *The Astrophys. J.* **643**, 923 (2006).

34. Ehrenfreund, P. *et al.* Laboratory studies of thermally processed H_2O-CH_3OH-CO_2 ice mixtures and their astrophysical implications. *Astron. & Astrophys.* **350**, 240–253 (1999).

35. Shkuratov, Y., Starukhina, L., Hoffmann, H. & Arnold, G. A Model of Spectral Albedo of Particulate Surfaces: Implications for Optical Properties of the Moon. *Icarus* **137**, 235–246, DOI: 10.1006/icar.1998.6035 (1999).

36. Brown, M. E., Schaller, E. L. & Fraser, W. C. A Hypothesis for the Color Diversity of the Kuiper Belt. *Astrophys. J. Lett.* **739**, L60, DOI: 10.1088/2041-8205/739/2/L60 (2011). 1109.0298.

37. Peixinho, N., Delsanti, A., Guilbert-Lepoutre, A., Gafeira, R. & Lacerda, P. The bimodal colors of Centaurs and small Kuiper belt objects. *Astron. & Astrophys.* **546**, A86, DOI: 10.1051/0004-6361/201219057 (2012). 1206.3153.

38. Peixinho, N., Delsanti, A. & Doressoundiram, A. Reanalyzing the visible colors of Centaurs and KBOs: what is there and what we might be missing. *A@AND@A* **577**, A35, DOI: 10.1051/0004-6361/201425436 (2015). 1502.04145.

39. Tegler, S. C., Romanishin, W., Consolmagno, G. J. & J., S. Two Color Populations of Kuiper Belt and Centaur Objects and the Smaller Orbital Inclinations of Red Centaur Objects. *Astron. J.* **152**, 210, DOI: 10.3847/0004-6256/152/6/210 (2016).

40. Marsset, M. *et al.* Col-OSSOS: Color and Inclination Are Correlated throughout the Kuiper Belt. *Astron. J.* **157**, 94, DOI: 10.3847/1538-3881/aaf72e (2019). 1812.02190.

41. Fraser, W. C. *et al.* Col-OSSOS: The Two Types of Kuiper Belt Surfaces. *arXiv e-prints* arXiv:2206.04068, DOI: 10.48550/arXiv.2206.04068 (2022). 2206.04068.

42. Dodson-Robinson, S. E., Willacy, K., Bodenheimer, P., Turner, N. J. & Beichman, C. A. Ice lines, planetesimal composition and solid surface density in the solar nebula. *Icarus* **200**, 672–693, DOI: 10.1016/j.icarus.2008.11.023 (2009). 0806.3788.

43. Nesvorný, D. & Morbidelli, A. Statistical Study of the Early Solar System's Instability with Four, Five, and Six Giant Planets. *Astron. J.* **144**, 117, DOI: 10.1088/0004-6256/144/4/117 (2012). 1208.2957.

44. Nesvorný, D. *et al.* OSSOS XX: The Meaning of Kuiper Belt Colors. *Astron. J.* **160**, 46, DOI: 10.3847/1538-3881/ab98fb (2020). 2006.01806.

45. Strazzulla, G., Cooper, J. F., Christian, E. R. & Johnson, R. E. Ion irradiation of tnos: from the fluxes measured in space to the laboratory experiments. *Comptes Rendus Physique* **4**, 791–801, DOI: https://doi.org/10.1016/j.crhy.2003.10.009 (2003). Dossier: New frontiers in the Solar System: trans-Neptunian objects.

46. Grundy, W. M. *et al.* Surface compositions across Pluto and Charon. *Science* **351**, aad9189, DOI: 10.1126/science.aad9189 (2016). 1604.05368.

47. Ahrens, C., Meraviglia, H. & Bennett, C. A Geoscientific Review on CO and CO2 Ices in the Outer Solar System. *Geosciences* **12**, 51, DOI: 10.3390/geosciences12020051 (2022).

48. Brucato, J. R., Palumbo, M. E. & Strazzulla, G. Carbonic acid by ion implantation in water/carbon dioxide ice mixtures. *Icarus* **125**, 135–144 (1997).

49. Mejía, C. *et al.* Radiolysis and sputtering of carbon dioxide ice induced by swift ti, ni, and xe ions. *Nucl. Instruments Methods Phys. Res. Sect. B: Beam Interactions with Mater. Atoms* **365**, 477–481 (2015).

50. Hénault, E. *et al.* Spectroscopic study of proton-irradiated water-methanol ice mixtures in support of tnos' and centaurs' observations. *44th COSPAR Sci. Assembly. Held 16-24 July* **44**, 245 (2022).

51. Bauer, J. M. *et al.* Centaurs and Scattered Disk Objects in the Thermal Infrared: Analysis of WISE/NEOWISE Observations. *Astrophys. J.* **773**, 22, DOI: 10.1088/0004-637X/773/1/22 (2013). 1306.1862.

52. Mommert, M. *et al.* TNOs are cool: A survey of the trans-Neptunian region. V. Physical characterization of 18 Plutinos using Herschel-PACS observations. *Astron. & Astrophys.* **541**, A93, DOI: 10.1051/0004-6361/201118562 (2012). 1202.3657.

53. Santos-Sanz, P. *et al.* "TNOs are Cool": A survey of the trans-Neptunian region. IV. Size/albedo characterization of 15 scattered disk and detached objects observed with Herschel-PACS. *Astron. & Astrophys.* **541**, A92, DOI: 10.1051/0004-6361/201118541 (2012). 1202.1481.

54. Kiss, C. *et al.* A portrait of the extreme solar system object 2012 DR_{30}. *Astron. & Astrophys.* **555**, A3, DOI: 10.1051/0004-6361/201321147 (2013). 1304.7112.

55. Lellouch, E. *et al.* "TNOs are Cool": A survey of the trans-Neptunian region. IX. Thermal properties of Kuiper belt objects and Centaurs from combined Herschel and Spitzer observations. *Astron. & Astrophys.* **557**, A60, DOI: 10.1051/0004-6361/201322047 (2013).

56. Fornasier, S. *et al.* TNOs are Cool: A survey of the trans-Neptunian region. VIII. Combined Herschel PACS and SPIRE observations of nine bright targets at 70-500 μm. *Astron. & Astrophys.* **555**, A15, DOI: 10.1051/0004-6361/201321329 (2013). 1305.0449.

57. Duffard, R. *et al.* "TNOs are Cool": A survey of the trans-Neptunian region. XI. A Herschel-PACS view of 16 Centaurs. *Astron. & Astrophys.* **564**, A92, DOI: 10.1051/0004-6361/201322377 (2014). 1309.0946.

58. Vilenius, E. *et al.* "TNOs are Cool": A survey of the trans-Neptunian region. X. Analysis of classical Kuiper belt objects from Herschel and Spitzer observations. *Astron. & Astrophys.* **564**, A35, DOI: 10.1051/0004-6361/201322416 (2014). 1403.6309.

59. Vilenius, E. *et al.* "tnos are cool": A survey of the trans-neptunian region - xiv. size/albedo characterization of the haumea family observed with herschel and spitzer. *A@AND@A* **618**, A136, DOI: 10.1051/0004-6361/201732564 (2018).

60. Müller, T., Lellouch, E. & Fornasier, S. Trans-Neptunian objects and Centaurs at thermal wavelengths. In Prialnik, D., Barucci, M. A. & Young, L. (eds.) *The Trans-Neptunian Solar System*, 153–181, DOI: 10.1016/B978-0-12-816490-7.00007-2 (2020).

61. Brucker, M. J. *et al.* High albedos of low inclination Classical Kuiper belt objects. **201**, 284–294, DOI: 10.1016/j.icarus.2008.12.040 (2009). 0812.4290.

62. Verbiscer, A. J. *et al.* The Diverse Shapes of Dwarf Planet and Large KBO Phase Curves Observed from New Horizons. **3**, 95, DOI: 10.3847/PSJ/ac63a6 (2022).

63. Bonett, D. G. & Wright, T. A. Sample size requirements for estimating pearson, kendall and spearman correlations. *Psychometrika* **65**, 23–28 (2000).

64. Rocha, W. *et al.* Lida: The leiden ice database for astrochemistry. *Astron. & Astrophys.* **668**, A63 (2022).

65. Ehrenfreund, P., Boogert, A. C. A., Gerakines, P. A., Tielens, A. G. G. M. & van Dishoeck, E. F. Infrared spectroscopy of interstellar apolar ice analogs. *Astron. & Astrophys.* **328**, 649–669 (1997).

66. Van Broekhuizen, F., Groot, I., Fraser, H., van Dishoeck, E. & Schlemmer, S. Infrared spectroscopy of solid co–co2 mixtures and layers. *Astron. & Astrophys.* **451**, 723–731 (2006).

67. Toplak, M., Read, S. T., Sandt, C. & Borondics, F. Quasar: easy machine learning for biospectroscopy. *Cells* **10**, 2300 (2021).

68. Speagle, J. S. DYNESTY: a dynamic nested sampling package for estimating Bayesian posteriors and evidences. *MNRAS* **493**, 3132–3158, DOI: 10.1093/mnras/staa278 (2020). 1904.02180.

69. Koposov, S. *et al.* joshspeagle/dynesty: v2.1.1, DOI: 10.5281/zenodo.7832419 (2023).

70. Skilling, J. Nested Sampling. In Fischer, R., Preuss, R. & Toussaint, U. V. (eds.) *Bayesian Inference and Maximum Entropy Methods in Science and Engineering: 24th International Workshop on Bayesian Inference and Maximum Entropy Methods in Science and Engineering*, vol. 735 of *American Institute of Physics Conference Series*, 395–405, DOI: 10.1063/1.1835238 (2004).

71. Skilling, J. Nested sampling for general Bayesian computation. *Bayesian Analysis* **1**, 833 – 859, DOI: 10.1214/06-BA127 (2006).

72. Baratta, G. & Palumbo, M. Infrared optical constants of co and co 2 thin icy films. *JOSA A* **15**, 3076–3085 (1998).

73. Mastrapa, R. M. *et al.* Optical constants of amorphous and crystalline H $_2$O-ice in the near infrared from 1.1 to 2.6 μm. *Icarus* **197**, 307–320, DOI: 10.1016/j.icarus.2008.04.008 (2008).

74. Mastrapa, R. M., Sandford, S. A., Roush, T. L., Cruikshank, D. P. & Dalle Ore, C. M. Optical Constants of Amorphous and Crystalline H_2O-ice: 2.5-22 μm (4000-455 cm^{-1}) Optical Constants of H_2O-ice. *Astrophys. J.* **701**, 1347–1356, DOI: 10.1088/0004-637X/701/2/1347 (2009).

75. Hudgins, D. M., Sandford, S. A., Allamandola, L. J. & Tielens, A. G. G. M. Mid- and Far-Infrared Spectroscopy of Ices: Optical Constants and Integrated Absorbances. *Astrophys. J. Suppl.* **86**, 713, DOI: 10.1086/191796 (1993).

76. Luna, R. *et al.* Densities, infrared band strengths, and optical constants of solid methanol. **617**, A116, DOI: 10.1051/0004-6361/201833463 (2018).

77. Khare, B. N. *et al.* Optical constants of organic tholins produced in a simulated Titanian atmosphere: From soft x-ray to microwave frequencies. *Icarus* **60**, 127–137, DOI: 10.1016/0019-1035(84)90142-8 (1984).

78. Dorschner, J., Begemann, B., Henning, T., Jaeger, C. & Mutschke, H. Steps toward interstellar silicate mineralogy. II. Study of Mg-Fe-silicate glasses of variable composition. *Astron. & Astrophys.* **300**, 503 (1995).

79. Hunter, J. D. Matplotlib: A 2d graphics environment. *Comput. Sci. & Eng.* **9**, 90–95, DOI: 10.1109/MCSE.2007.55 (2007).

80. McKinney, W. *et al.* Data structures for statistical computing in python. In *Proceedings of the 9th Python in Science Conference*, vol. 445, 51–56 (Austin, TX, 2010).

81. De Pra, M., Carvano, J., Morate, D., Licandro, J. & Pinilla-Alonso, N. Cana: An open-source python tool to study hydration in the solar system (2018).

82. Harris, C. R. *et al.* Array programming with NumPy. *Nature* **585**, 357–362, DOI: 10.1038/s41586-020-2649-2 (2020).

83. Virtanen, P. *et al.* SciPy 1.0: Fundamental Algorithms for Scientific Computing in Python. *Nat. Methods* **17**, 261–272, DOI: 10.1038/s41592-019-0686-2 (2020).

84. Community, E. B. Jupyter book, DOI: 10.5281/zenodo.4539666 (2020).

Acknowledgements

The DiSCo-TNOs team would like to thank Weston Eck and Alaina Henry of STScI for their help in preparing the observations for execution; Bret Blacker for his almost invisible and always helpful presence from submission to publication at the STScI office, and the Time Allocation and Executive Committees of the JWST because their generous effort and good work is essential for the scientific success of this impressive telescope. This work is based on observations made with the NASA/ESA/CSA James Webb Space Telescope. The data were obtained from the Mikulski Archive for Space Telescopes at the Space Telescope Science Institute, which is operated by the Association of Universities for Research in Astronomy, Inc., under NASA contract NAS 5-03127 for JWST. These observations are associated with program #2418. Support for program #2418 was provided by NASA through a grant from the Space Telescope Science Institute. This work is based on the use of several open-source Python programming language tools[67,79–84]. NP acknowledges funding by Fundação para a Ciência e a Tecnologia (FCT) through the research grants UIDB/04434/2020 and UIDP/04434/2020.

Author contributions statement

MDP performed the statistical analysis, compositional models, and overall analysis and interpretation of results. EH performed the calculation of band parameters, comparison with laboratory data, and overall analysis and interpretation of results. NPA, BJH, RB, and ACSF contributed significantly to the discussion and interpretation of the results. TM provided size, albedo and temperature calculation. All other authors reviewed the manuscript and contributed to the discussion of results.